**Rare Metal Materials and Engineering**
Volume 53, Issue 4, April 2024
Available online at www.rmme.ac.cn

Science Press

**Cite this article as**: Liu Guozheng, Zhao Yongqing, Jia Weiju, et al. Effect of Single Annealing and Multiple Heat Treatment on Fracture Toughness of Ti-5321 Alloy Prepared by Laser Cladding Forming[J]. Rare Metal Materials and Engineering, 2024, 53(04): 970-977. DOI: 10.12442/j.issn.1002-185X.20230498.

ARTICLE

# Effect of Single Annealing and Multiple Heat Treatment on Fracture Toughness of Ti-5321 Alloy Prepared by Laser Cladding Forming

**Liu Guozheng[1,2], Zhao Yongqing[1,2], Jia Weiju[2], Zhang Yan[1,2], Song Shuo[1,2], Mao Chengliang[2], Zhou Wei[2]**

*[1] Northeastern University, Shenyang 110819, China; [2] Northwest Institute for Nonferrous Metal Research, Xi'an 710016, China*

**Abstract:** In order to satisfy the requirements of aerospace field for rapid preparation of high strength and toughness complex titanium alloy parts, new Ti-5321 (Ti-5Al-3Mo-3V-2Zr-2Cr-1Nb-1Fe) alloy with high strength and high toughness was prepared by laser cladding forming, which possesses the superiority of rapid prototyping, high efficiency, and good formability. Through single annealing and multiple heat treatment ($\beta$-annealing with slow cooling and aging, BASCA) on Ti-5321 alloy, the microstructure evolution was revealed, and the influence of different microstructures on the fracture toughness was explored. Results show that after single annealing, the alloy morphology presents the basket-weave structure consisting of elongated lamellar $\alpha$ phases. Its ultimate tensile strength is 1102 MPa, and fracture toughness is 68.1 MPa·m$^{1/2}$. After BASCA heat treatment, the elongated lamellar $\alpha$ phase changes to coarse lamellar $\alpha$ phase and ultrafine needle-like $\alpha$ phase. Thus, the ultimate tensile strength increases to 1309 MPa, whereas the fracture toughness reduces to 45.5 MPa·m$^{1/2}$. BASCA heat treatment can enhance the strength but degrade the toughness of alloys. This is because the elongated lamellar $\alpha$ phase in basket-weave structure can greatly increase the crack growth resistance and aggravate the tortuous degree of crack growth path, thus improving the alloy toughness. Coarse lamellar $\alpha$ phase after BASCA heat treatment has a certain degree of directionality, and the cracks only deflect when passing through the coarse lamellar $\alpha$ phase of different $\beta$ grains. Crack propagation mainly occurs in the ultrafine needle-like $\alpha$ phase. However, due to the extremely small size of ultrafine needle-like $\alpha$ phase, it cannot hinder the development of crack path or deflect the cracks. Thus, the toughness of coarse lamellar structure becomes more inferior after BASCA heat treatment.

**Key words:** laser cladding forming; Ti-5321 alloy; multiple heat treatment; fracture toughness

Because of its advantages of high strength, good corrosion resistance, and high plasticity, titanium alloy with high strength and high toughness is widely used in aerospace, medical equipment, and petrochemical fields[1]. Currently, the basic definition of high strength and high toughness for titanium alloys is that the ultimate tensile strength (UTS) is higher than 1000 MPa and the fracture toughness is greater than 55 MPa·m$^{1/2}$[2]. Therefore, titanium alloys with high strength and high toughness mainly include the near $\beta$ titanium alloy[3–4], metastable $\beta$ titanium alloy[5], and $\alpha+\beta$ titanium alloy[6]. For example, Ti-5553 alloy[7] is designed based on BT22 alloy[8], Ti-55531 alloy[9], Ti1300 alloy[10], Ti-62222s alloy[11], and TC21 alloy[12–13]. These alloys are normally used in the manufacture of new aircraft. Referring to the element composition of Ti-1300 and TC21 alloys, a new titanium alloy with high strength and high toughness, Ti-5321 (Ti-5Al-3Mo-3V-2Zr-2Cr-1Nb-1Fe) alloy, has been designed and developed[14–17]. Ti-5321 alloy is a metastable titanium alloy with a large range of structure and property regulation.

With the development of industrial technology and the improvement in industrial requirements, higher requirement is proposed for the application of titanium alloys with high strength and high toughness: rapid manufacture. Traditional manufacture techniques of titanium alloys with high strength

Received date: August 14, 2023
Foundation item: National Key Technologies Research and Development Program of China (2021YFC2801901)
Corresponding author: Zhao Yongqing, Ph. D., Professor, Northwest Institute for Nonferrous Metal Research, Xi'an 710016, P. R. China, Tel: 0086-29-86250729, E-mail: trc@c-nin.com

Copyright © 2024, Northwest Institute for Nonferrous Metal Research. Published by Science Press. All rights reserved.

and high toughness have the disadvantages of high cost, long processing cycle, and low precision[18]. Additive manufacturing (AM) [19–20], such as selective laser melting (SLM) [21–22], laser melting deposition[23], and laser cladding forming (LCF), can solve the shortcomings of traditional processing methods. LCF of Ti-5321 alloy cannot only rapidly form complex components, but also satisfy the design requirements of lightweight, convenience, and efficiency. Additionally, the unique thermal cycle and processing characteristics of titanium alloys may control the microstructures and properties[24]. Through heat treatment[25–26], the alloy microstructure can be further optimized to achieve equivalent or better performance[27]. For example, after annealing at 500 ° C, Ti-5553 (Ti-5Al-5Mo-5V-3Cr) alloy prepared by SLM technique has the microstructure of $\beta$ phase matrix and uniformly dispersed lamellar $\alpha$ phase, and its UTS increases to 1600 MPa[28]. Similarly, bimodal and bi-lamellar microstructures can be obtained after certain heat treatments: Ti-55531 alloy after heat treatment possesses significantly refined primary $\alpha$ phase precipitates within the $\beta$ grains. SLM technique is expected to eliminate the anisotropy and to improve the corrosion resistance of Ti-55531 alloy[29]. Similar to Ti-5553 alloy, Ti-55511 (Ti-5Al-5Mo-5V-1Cr-1Fe) alloy is also very sensitive to the heat treatment mechanism due to the microstructure evolution and fracture toughness. The increase in aging temperature results in coarser $\alpha$ phase, reduces its content, deflects the crack, and consumes additional energy, thus improving the fracture toughness. Liu et al[30] proved that the microstructure evolution and fracture toughness of Ti-55511 alloy are very sensitive to the multiple heat treatment mechanism. Multiple heat treatment is an extension of single annealing heat treatment, and it is one of the main methods to adjust the microstructure of titanium alloys. Furuhara et al[31] improved the strength-toughness balance of $\beta$-Ti-15-3 alloy by a specially designed high-low temperature two-step aging treatment. Although the heat treatment methods and their influence on titanium alloys are similar, the relationship among heat treatment, microstructure, and fracture toughness should be further investigated. In this research, the effect of heat treatment on the microstructure of Ti-5321 alloy was investigated, and the effect of different microstructures on the mechanical properties and fracture toughness of the alloy was analyzed. This research provides reference for the subsequent investment of titanium alloys with high strength and high toughness.

## 1 Experiment

The raw material for LCF manufacture was Ti-5321 alloy powder, and its chemical composition is shown in Table 1. The phase transformation temperature is 865 ° C. The morphology of Ti-5321 alloy powder was observed by scanning electron microscope (SEM). Fig. 1 shows SEM morphologies of Ti-5321 alloy powder. No binding or agglomeration phenomenon exists in the powder. No “satellite powder” can be observed, and all powder particles maintain good sphericity. The surface of alloy powder is free of holes, cracks, or any other defects, and the interior of alloy powder is compact. The particle size of alloy powder was measured by Image Pro Plus 6.0 software, The particle diameter is mainly 80–110 μm, and the median particle diameter is 100 μm.

**Table 1 Chemical composition of Ti-5321 alloy powder (wt%)**

| Al | Mo | V | Zr | Cr | Nb | Fe | O | Ti |
|---|---|---|---|---|---|---|---|---|
| 5.05 | 2.96 | 2.96 | 1.88 | 1.99 | 0.96 | 0.99 | 0.091 | Bal. |

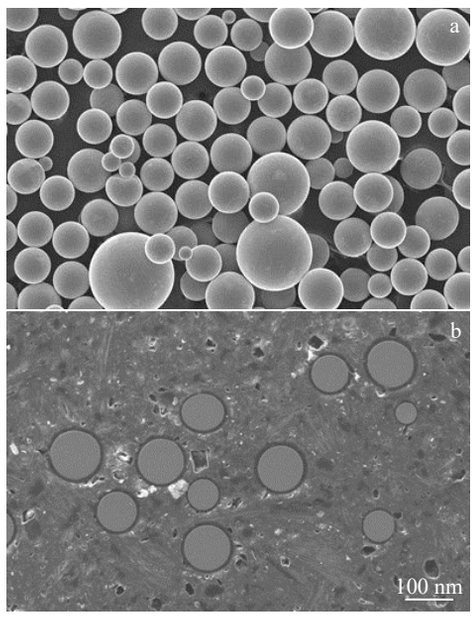


Fig.1 SEM surface (a) and interior (b) morphologies of Ti-5321 alloy powder

Ti-5321 alloy was prepared by LCF equipment. LCF equipment is composed of laser device, powder feeder, water cooling device, control cabinet, powder feeding nozzle, forming workbench, and protective atmosphere. LCF preparation parameters are shown in Table 2.

In order to reduce the residual stress in the component, the as-prepared components should be immediately heat-treated. The single annealing process was conducted at 530 °C for 1 h with air cooling (AC). The multiple heat treatment involved the processes of heating to 880 °C, holding at 880 °C for 1 h, cooling to 800 ° C in the two-phase zone at furnace cooling rate of 0.5 °C/min, then AC to room temperature, and finally aging at 580 °C for 6 h with AC. This multiple heat treatment is also denoted as $\beta$-annealing with slow cooling and aging (BASCA) treatment. Thus, the Ti-5321 alloy specimens after single annealing and multiple heat treatment are named as S-A and S-B specimens, respectively. The tensile properties at

**Table 2 LCF preparation parameters**

| Parameter | Value |
|---|---|
| Laser power, $P$/kW | 6–8 |
| Scanning speed, $v$/mm·min$^{-1}$ | 800–1200 |
| Powder feeding speed, $v_f$/g·h$^{-1}$ | 1000–1200 |
| Overlap ratio, $r$/% | 30–50 |

room temperature and fracture toughness of S-A and S-B specimens were tested, and the effect of microstructure on the mechanical properties and fracture toughness of the alloy was analyzed by optical microscope (OM) and SEM. Tensile test at room temperature was conducted by Instron 1195 universal electronic testing machine. The fracture toughness test was conducted by MTS 370.10 low-cycle fatigue testing machine. The fatigue crack with length of about 1.5 mm was prefabricated with stress ratio of $R$=0.1. Fig. 2 shows the specimen position and dimension.

## 2 Results and Discussion

### 2.1 Microstructure

OM morphology of S-A specimen is shown in Fig. 3a. The intragranular $\alpha$ phase has thin long needle-like lamellar morphology, and it is interlaced and woven into basket shape, namely basket-weave structure. Fig. 3b shows OM morphology of S-B specimen, which consists of elongated $\alpha$ phase. The needle-like $\alpha$ phase completely disappears and changes into thick lamellar $\alpha$ phase. The coarse lamellar $\alpha$ phases have certain directionality, but the coarse lamellar $\alpha$ phases in different $\beta$ grains have nonuniformity.

Fig. 4a shows SEM microstructure of S-A specimen. The black elongated needle-like or lamellar $\alpha$ phase is uniformly distributed on the white $\beta$ phase matrix, forming the basket-weave structure. Fig. 4b shows SEM microstructure of S-B specimen. With large size and uniform orientation, the discontinuous lamellar $\alpha$ phase remains parallel in $\beta$ grains. Ultrafine needle-like $\alpha$ phases exist between coarse lamellar $\alpha$ phases. The width of ultrafine needle-like $\alpha$ phase is only 0.1 μm, resulting in high brittleness, which may cause great damage to the fracture toughness of the organization.

### 2.2 Mechanical properties

After conducting tensile tests at room temperature, the tensile properties of S-A and S-B specimens are shown in Table 3. Three groups of tensile tests were conducted, and the group with the largest deviation of test data was eliminated to reduce the error caused by the inhomogeneity of AM organization. The yield strength of S-A specimen is 1032 MPa, UTS is 1102 MPa, the elongation after fracture is 13.5%, and the area reduction is 26%. The yield strength of S-B specimen is 1228 MPa, UTS is 1309 MPa, the elongation after fracture reduces to 6.5%, and the area reduction is 13%. Fig. 5 shows the engineering stress-strain curves of S-A and S-B specimens. Compared with that of S-A specimen, the strength of S-B specimen greatly improves, which is attributed to the significant increase in yield strength and UTS. Besides, the plasticity, elongation, and area reduction all decrease after

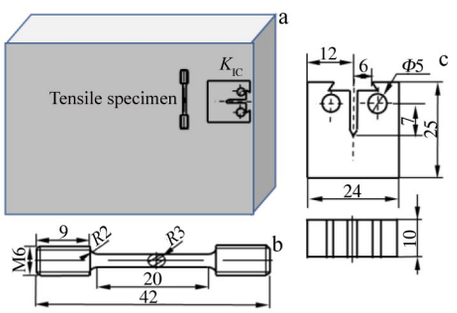


Fig.2 Schematic diagrams of specimen position (a), tensile specimen (b), and fracture toughness specimen (c)

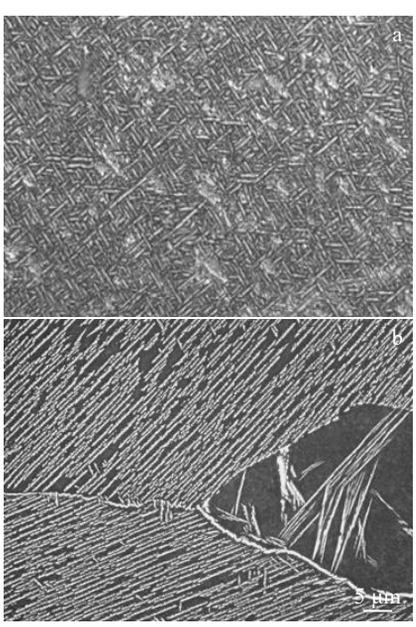


Fig.3 OM microstructures of S-A (a) and S-B (b) specimens

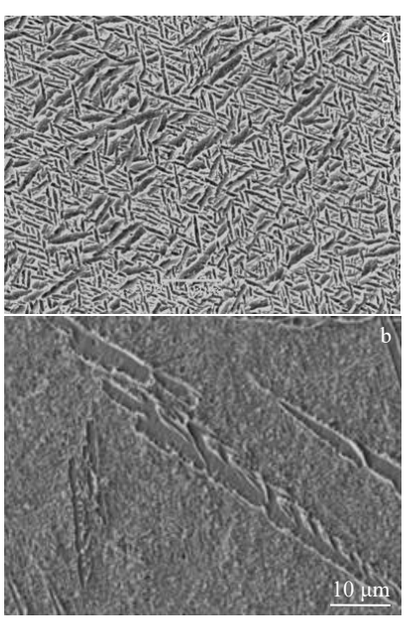


Fig.4 SEM microstructures of S-A (a) and S-B (b) specimens

**Table 3 Tensile properties of S-A and S-B specimens**

| Specimen | UTS/MPa | Yield strength/MPa | Elongation/% | Area reduction/% |
|---|---|---|---|---|
| S-A | 1102 | 1032 | 13.5 | 26 |
| S-B | 1309 | 1228 | 6.5 | 13 |

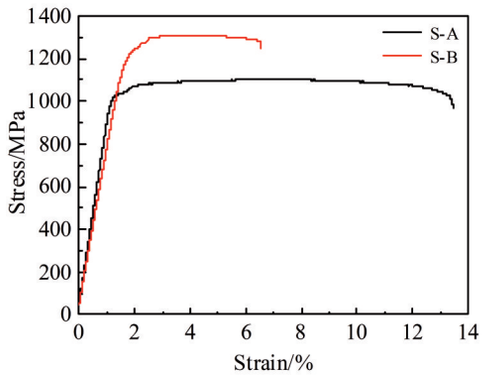


Fig.5 Engineering stress-strain curves of S-A and S-B specimens at room temperature

BASCA treatment.

Fig.6 shows SEM morphologies of S-A and S-B specimens after tensile fracture. It can be found that the fracture types of the two specimens are similar. The fracture is characterized by ductile fracture, and the fracture area can be divided into fibrous zone and shear lip zone. There are a lot of microvoids in the dimple, and the micropores are free of inclusions. Thus, it can be judged that the fracture mechanism is microporous aggregation fracture. The fibrous zone shape of S-B specimen is regular, and many cleavage surfaces and large size dimples exist on the S-B specimen. The shear lip zone is smoother and the dimples are smaller, which indicates that S-B specimen has brittle fracture characteristics. The strength of S-B specimen is higher than that of S-A specimen, but the toughness of S-B specimen is worse.

### 2.3 Fracture toughness

In the fracture toughness tests, the specimens with small thickness were selected to measure the fracture toughness. Table 4 shows the fracture toughness of S-A and S-B specimens. Among them, $2.5(F_Q/R_{P0.2})^2$ represents effective toughness criteria, $F_Q$ is the stress field strength factor, $R_{P0.2}$ is the yield strength, and $a$ is the crack length. The fracture toughness $K_Q$ of S-A and S-B specimens is 68.1 and 45.5 MPa·m$^{1/2}$, respectively. S-A specimen has higher fracture toughness. It is inferred that the size and morphology of $\alpha$ phase can affect the strength and toughness of Ti-5321 alloy.

Fracture toughness is closely related to the crack propagation. The tortuous crack path reduces the effective crack driving force on the crack tip, increases the crack propagation resistance, and improves the fracture toughness. The fracture morphology of S-A specimen has two typical regions: the pre-crack region (PR) and the unstable crack propagation region (UCPR), as shown in Fig. 7a. The crack propagation path in PR is relatively straight and the area is small and flat. Obvious smooth cleavage surface can be observed. Ductile bands and shear lips can be observed in UCPR of S-A specimen. The crack propagation path is tortuous and undulating. The fracture morphology of S-B specimen is more gentle. No significant transition region exists between PR and UCPR, and the shear lip zone is small, as shown in Fig.7b.

Fig.8 shows SEM morphologies of S-A and S-B specimens after fracture. The fracture morphologies can be divided into three typical areas: PR, UCPR, and transition region. The overall appearance shows typical fatigue fracture characteristics. A large number of cleavage steps, river patterns, and small secondary cracks can be observed in PR. The front end of the transition region is characterized by cleavage surface and microcracks, which form a clear boundary with the tearing edge and the dimples of UCPR at the rear end. Larger and deeper tearing edges appear and the

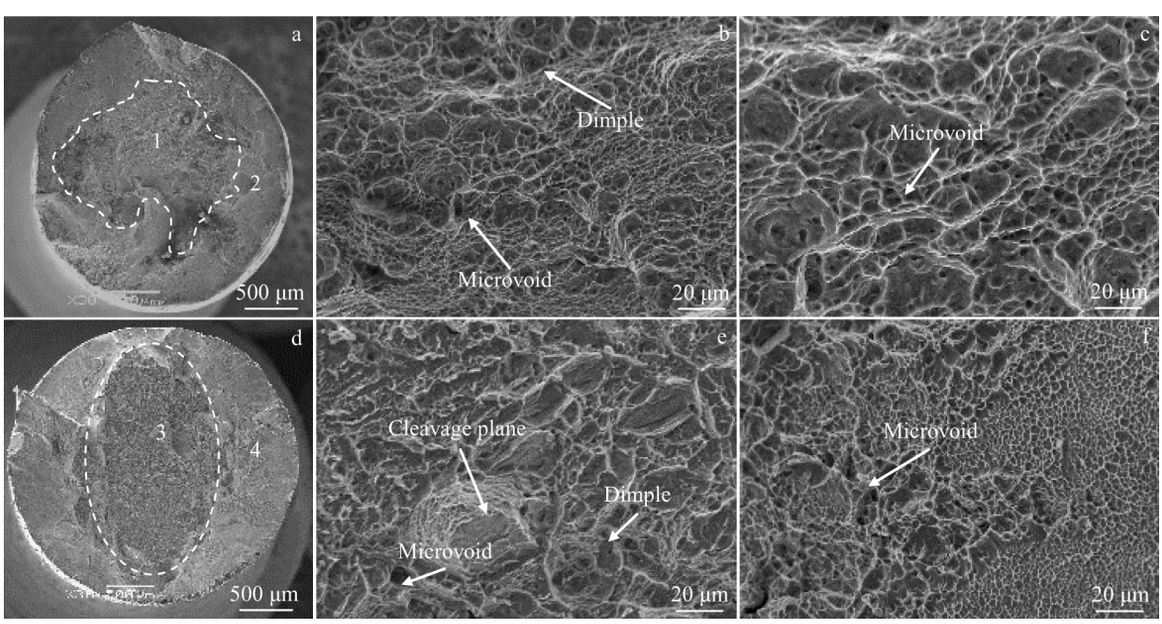


Fig.6 SEM morphologies of S-A (a) and S-B (d) specimens after tensile fracture; magnified images of area 1 (b) and area 2 (c) in Fig. 6a; magnified images of area 3 (e) and area 4 (f) in Fig.6d

**Table 4 Fracture toughness of S-A and S-B specimens**

| Specimen | Fracture toughness, $K_Q$/MPa·m$^{1/2}$ | Effective toughness criteria, $2.5(F_Q/R_{P0.2})^2$/mm | Crack length, $a$/mm |
|---|---|---|---|
| S-A | 68.1 | 11.59 | 10.106 |
| S-B | 45.5 | 3.40 | 9.797 |

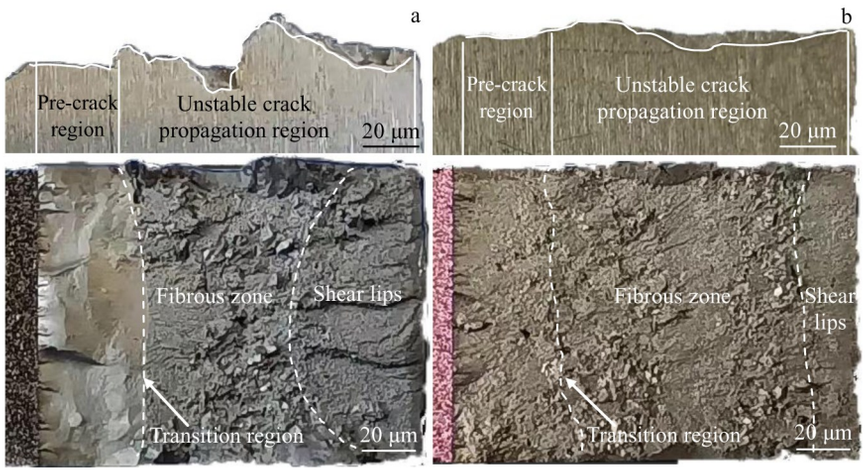


Fig.7 Fracture appearances of S-A (a) and S-B (b) specimens

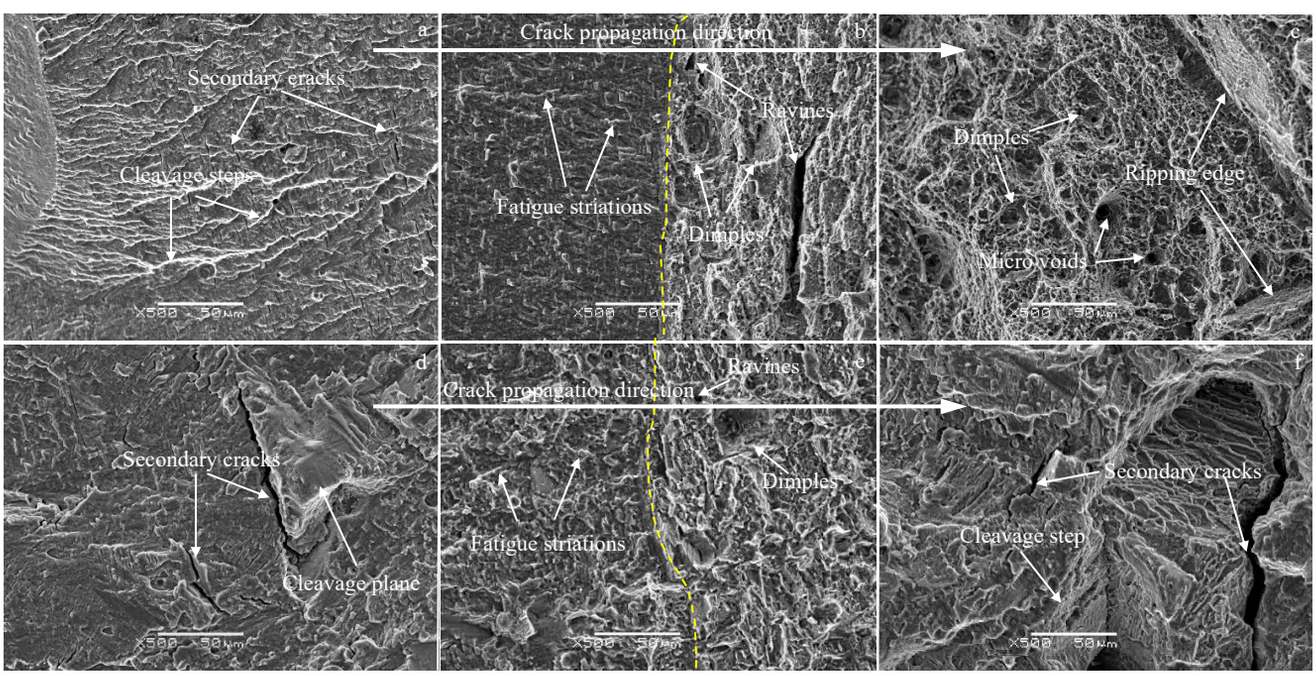


Fig.8 SEM microstructures of S-A (a–c) and S-B (d–f) specimens after fracture along the crack propagation direction

secondary cracks cause rough surfaces. These phenomena present the complete static tensile fracture characteristics. As shown in Fig.8d, the fracture morphology of S-B specimen is also composed of three areas: PR, UCPR, and transition region. However, PR of S-B specimen has more cleavage surfaces and cleavage steps, and the size of the secondary cracks is larger. The transition region is less obvious. UCPR presents more obvious brittle fracture characteristics, which is basically composed of cleavage surface, cleavage steps, and a large number of the secondary cracks with large size. Obvious dimples cannot be observed in the S-B specimen. These results also prove that the toughness of S-B specimen is inferior.

### 2.4 Discussion

#### 2.4.1 Microstructural morphology

Fig.9 shows the size of $\alpha$ phases in S-A and S-B specimens. The length of the lamellar $\alpha$ phase in S-A specimen is 2–4 μm, the width is 0.4–0.6 μm, and the aspect ratio is about 5. The length of the lamellar $\alpha$ phase in S-B specimen is 10–30 μm,

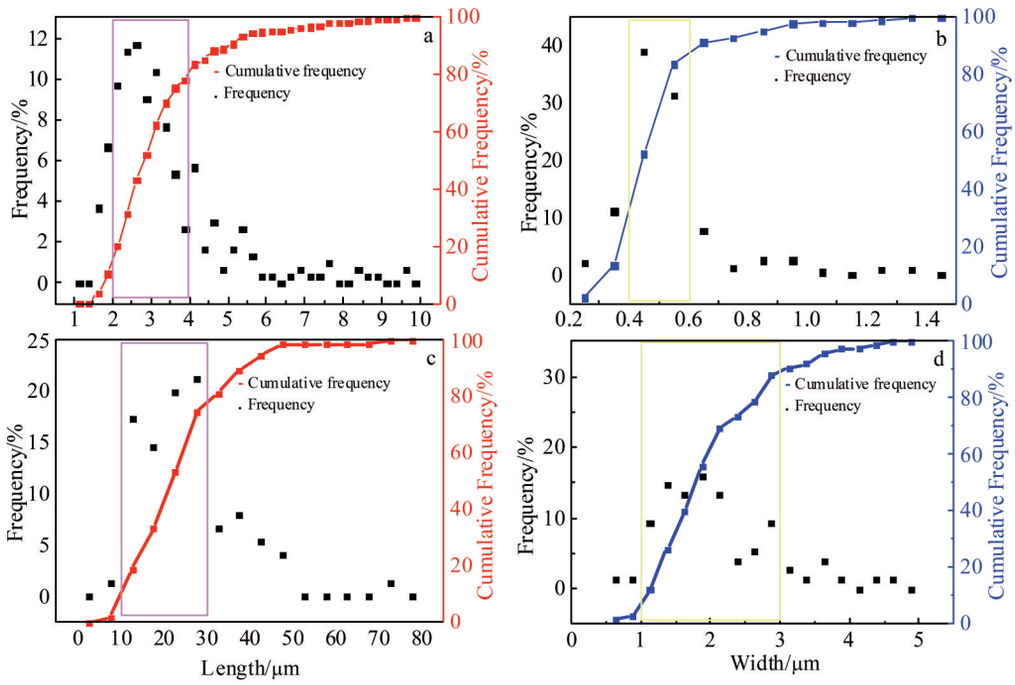


Fig.9 Length (a, c) and width (b, d) of lamellar $\alpha$ phase in S-A (a–b) and S-B (c–d) specimens

the width is 1–3 μm, and the aspect ratio is about 10. It can be seen that the size and aspect ratio of $\alpha$ phase in S-B specimen are much larger than those of S-A specimen.

During the multiple heat treatment process of Ti-5321 alloy, the insulation treatment in the single $\beta$ phase zone completely dissolves the lamellar $\alpha$ phase, forming the metastable $\beta$ phase. When the alloy slowly cools from the $\beta$ single phase zone to the $\alpha$+$\beta$ dual-phase zone, the cooling rate is small, the cooling time is short, and the undercooling degree is small. The crystal nuclei are firstly formed at the grain boundary and then connected, forming the continuous grain boundaries. The $\alpha$ phase gradually grows into the crystal, forming coarse lamellar $\alpha$ phase. During the subsequent long-term aging process, a large amount of ultrafine needle-like $\alpha$ phase is precipitated.

2.4.2 Load-displacement curves

Load-displacement (*F*-*V*) curves of S-A and S-B specimens are as shown in Fig.10. For S-A specimen, there is an obvious

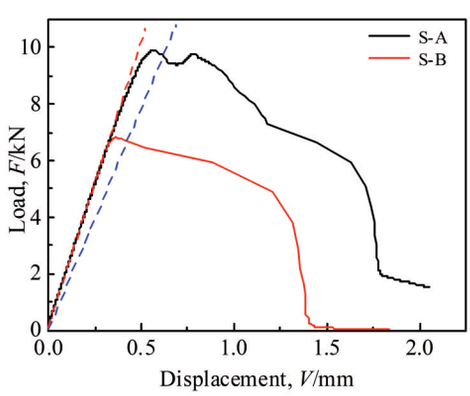


Fig.10 Load-displacement curves of S-A and S-B specimens

"burst" platform. This is because the crack tip is unstable and the cracks are propagated firstly. The surface layer produces plastic deformation, forming a plastic zone at the crack tip, which causes the crack growth in the center. It is necessary to apply more load to destroy the plastic zone, so the load needs to be increased to promote the crack growth. These results show that S-A specimen has good toughness. However, the *F*-*V* curve of S-B specimen does not have such platform, and no plastic deformation zone occurs at the crack tip, indicating that toughness of S-B specimen is inferior.

2.4.3 Crack propagation path

The crack propagation path of S-A specimen is shown in Fig. 11a. The crack growth path in PR is relatively smooth, whereas the crack growth path in UCPR greatly fluctuates. The secondary cracks can be observed in UCPR. Intragranular crack propagation mainly has three forms: segment 1 (S1) along the $\alpha$ phase extension; segment 2 (S2) of oblique propagation through $\alpha$ phase; segment 3 (S3) of vertical propagation through $\alpha$ phase. According to Fig. 11e and 11f, there are three types of crack propagation segments in S-A and S-B specimens, respectively, which mainly include the S2 and S3. The crack propagation segments of S-A specimens are composed of continuous S1, S2, and S3. When the crack crosses different $\alpha$ phases, it deflects to a certain extent. Therefore, the crack propagation path has many small twists and turns, and the crack propagation is hindered, improving the toughness. In S-B specimen, the crack propagation mainly occurs in the ultrafine needle-like $\alpha$ phase. The crack propagation path is smooth without twists and turns, as shown in Fig.11d. This is because the ultrafine needle-like $\alpha$ phase cannot hinder the crack growth, therefore degrading the alloy toughness. Only when the crack is propagated to the coarse lamellar $\alpha$ phase, the crack deflects to a certain degree. In this case, the crack

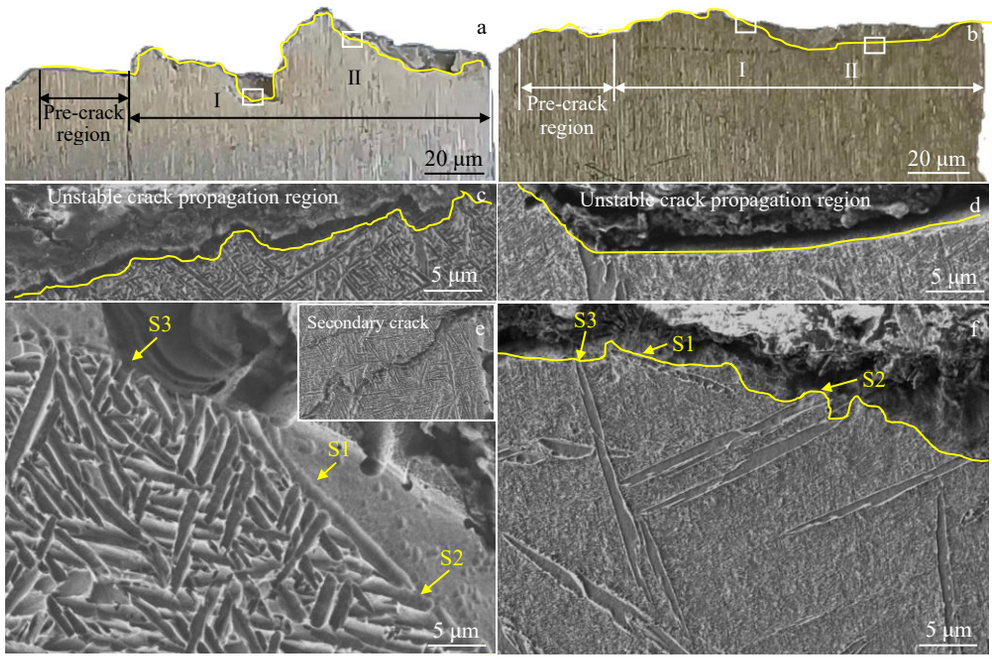


Fig.11 Crack propagation paths of S-A (a) and S-B (b) specimens after tensile fracture; magnified images of area I (c) and area II (d) in Fig.11a; magnified images of area I (e) and area II (f) in Fig.11b

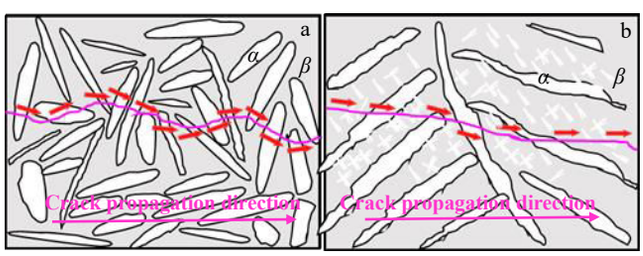


Fig.12 Schematic diagrams of crack propagation of S-A (a) and S-B (b) specimens during fracture process

propagation is hindered, improving the alloy toughness.

According to the morphologies and crack propagation path of S-A (basket-weave structure) and S-B (coarse lamellar structure) specimens, the crack propagation models of Ti-5321 titanium alloy prepared by LCF technique are established, as shown in Fig.12. The cracks in the basket-weave structure are propagated through $\alpha$ phase. When the cracks are propagated between different $\alpha$ phases, they deflect at a certain angle. Thus, the resistance against crack propagation is large and the fracture toughness is good. In the coarse lamellar structure, when the cracks cross through the ultrafine needle-like $\alpha$ phase, the crack propagation has no deflection. When the cracks cross through the coarse lamellar $\alpha$ phase, the crack propagation has a certain degree of deflection. Therefore, the toughness of coarse lamellar structure is inferior.

## 3 Conclusions

1) After single annealing process, the Ti-5321 alloy prepared by LCF technique has basket-weave structure, which is composed of elongated lamellar $\alpha$ phase. After multiple heat treatment, the microstructure of Ti-5321 alloy consists of coarse lamellar $\alpha$ phase and ultrafine needle-like $\alpha$ phase.

2) After single annealing process, the plasticity and toughness of Ti-5321 alloy are enhanced. After multiple heat treatment, the plasticity and toughness of Ti-5321 alloy decrease, but the strength significantly increases.

3) After single annealing process, the plastic zone of crack tip is generated during the crack propagation, which increases the resistance against the crack propagation, thereby hindering the crack propagation. After multiple heat treatment, there is no plastic zone at the crack tip, and Ti-5321 alloy exhibits brittle fracture characteristics.

4) After different heat treatments, the crack propagation modes are similar: through $\alpha$ phase and along $\alpha$ phase. The morphology and size of $\alpha$ phase affect the alloy toughness. After single annealing process, deflection occurs when the cracks cross through different $\alpha$ phases. The crack propagation path has more twists and turns, and the crack propagation resistance increases, which improves the toughness of Ti-5321 alloy. After multiple heat treatment, crack propagation mainly occurs in the ultrafine needle-like $\alpha$ phase. But the ultrafine $\alpha$ phase is brittle and cannot prevent the crack growth. Thus, the toughness of Ti-5321 alloy is inferior.

5) This research provides reference for the rapid manufacture of new titanium alloys with high strength and high toughness, presenting guidance for the control of microstructure and properties.

## References

1 Huang Boyun, Li Chenggong, Shi Likai *et al*. *China Materials Engineering Canon*[M]. Beijing: Chemical Industry Press, 2006:

503 (in Chinese)
2 Yang Dongyu, Fu Yanyan, Hui Songxiao *et al*. *Chinese Journal of Rare Metals*[J], 2011, 35(4): 575 (in Chinese)
3 Zhang Haoyu, Wang Chuan, Liu Dan *et al*. *Rare Metal Materials and Engineering*[J], 2022, 51(6): 2137 (in Chinese)
4 Dipankar B, Williams J C. *Acta Materialia*[J], 2013, 61(3): 844
5 Zhu W G, Lei J, Su B *et al*. *Materials Science and Engineering A*[J], 2020, 782: 139248
6 Wu Jingyi, Yang Liu, Dai Guanglin *et al*. *Rare Metal Materials and Engineering*[J], 2022, 51(2): 615 (in Chinese)
7 Zhou Wei, Ge Peng, Li Qian *et al*. *Rare Metal Materials and Engineering*[J], 2016, 45(7): 1732 (in Chinese)
8 Oleksandr T, Magdalena L, Yurii T *et al*. *Metals*[J], 2022, 12(1): 100
9 Zhang Qifei, Yang Shuai, Liu Shujun *et al*. *Rare Metal Materials and Engineering*[J], 2022, 51(7): 2645 (in Chinese)
10 Ma Quan, Xin Shewei, Song Kai *et al*. *Rare Metal Materials and Engineering*[J], 2019, 48(8): 2723 (in Chinese)
11 Weiss I, Semiatin S L. *Materials Science and Engineering A*[J], 1998, 243(1–2): 46
12 Sun Yue, Sun Yong, Yang Yong *et al*. *Rare Metal Materials and Engineering*[J], 2023, 52(9): 3139 (in Chinese)
13 Qin Haixu, Geng Naitao, Yang Liu *et al*. *Titanium Industry Progress*[J], 2023, 40(3): 6 (in Chinese)
14 Ren L, Xiao W L, Chang H *et al*. *Materials Science and Engineering A*[J], 2018, 711: 553
15 Wu C, Zhao Q Y, Huang S X *et al*. *Journal of Materials Science & Technology*[J], 2022, 112(17): 36
16 Wang H, Xin S W, Zhao Y Q, *et al*. *Materials Science and Engineering A*[J], 2020, 797: 140080
17 Wu C, Zhao Y Q, Huang S X *et al*. *Materials Characterization*[J], 2021, 175: 111103
18 Wang Huaming. *Acta Aeronautica et Astronautica Sinica*[J], 2008, 23(5): 473 (in Chinese)
19 Yang Junwei, Tang Haibo, Tian Xiangjun *et al*. *Rare Metal Materials and Engineering*[J], 2023, 52(9): 3316 (in Chinese)
20 Guo Yanhua, Dai Guoqing, Sun Zhonggang *et al*. *Rare Metal Materials and Engineering*[J], 2022, 51(12): 4733 (in Chinese)
21 Aufa A N, Hassan M Z, Ismail Z. *Journal of Alloys and Compounds*[J], 2022, 896: 163072
22 Lu J W, Zhuo L C. *International Journal of Refractory Metals and Hard Materials*[J], 2023, 111: 106110
23 Qin L Y, Men J H, Zhang L S *et al*. *Materials Science and Engineering A*[J], 2019, 759: 404
24 Zhang T L, Liu C T. *Advanced Powder Materials*[J], 2022, 1(1): 100014
25 Zhang Mingyu, Yun Xinbing. *Rare Metal Materials and Engineering*[J], 2023, 52(5): 1759 (in Chinese)
26 Liu Sinong, Zhang Jingqi, Liu Bowei *et al*. *Rare Metal Materials and Engineering*[J], 2023, 52(10): 3485 (in Chinese)
27 Majid L, Esmaeil S, Reynier I R *et al*. *Progress in Materials Science*[J], 2023, 133: 101051
28 Holger S, Matthias B, Lars G *et al*. *Materials & Design*[J], 2017, 130: 83
29 Zuo H Y, Deng H, Zhou L J *et al*. *Surface and Coatings Technology*[J], 2022, 445: 128743
30 Liu Z D, Du Z X, Jiang H Y *et al*. *Journal of Materials Research and Technology*[J], 2022, 17: 2528
31 Furuhara T, Maki T, Makino T. *Journal of Materials Processing Technology*[J], 2001, 117(3): 318

# 简单退火和多重热处理对激光熔覆成形 Ti-5321 合金断裂韧性的影响

刘国政[1,2]，赵永庆[1,2]，贾蔚菊[2]，张　艳[1,2]，宋　硕[1,2]，毛成亮[2]，周　伟[2]
(1. 东北大学，辽宁 沈阳 110819)
(2. 西北有色金属研究院，陕西 西安 710016)

**摘　要：**为满足航空航天领域对快速制备高强韧复杂钛合金零件的需求，采用激光熔覆成形新型高强韧Ti-5321（Ti-5Al-3Mo-3V-2Zr-2Cr-1Nb-1Fe）合金，具有成形快、效率高、成形构件性能良好等优势。通过对Ti-5321合金进行简单退火和多重热处理（$\beta$相区固熔缓冷加时效，BASCA），揭示了其显微组织的演变规律，并探究不同组织对断裂韧性的影响。结果表明：简单退火后，合金呈细长针片状$\alpha$交织成的网篮组织，其抗拉伸强度为1102 MPa，断裂韧性为68.1 MPa·m$^{1/2}$。经BASCA热处理后，细长针片状$\alpha$相全部转变为粗大的片层$\alpha$相和超细针状$\alpha$相，且合金的抗拉伸强度提高至1309 MPa，而断裂韧性降低至45.5 MPa·m$^{1/2}$。BASCA热处理能够提高合金强度，但会降低合金韧性。这是由于网篮组织中细长的针片状$\alpha$相能够大大增加裂纹扩展阻力，增大裂纹扩展路径曲折程度，从而提高合金的韧性。而BASCA热处理组织中大片层$\alpha$相具有一定的方向性，裂纹只有在穿过不同$\beta$晶粒的大片层$\alpha$相时才会发生偏转；且裂纹扩展主要发生在超细针状$\alpha$相中，而超细针状$\alpha$相尺寸过于细小，不能阻碍裂纹的发展或使裂纹偏转，因此经BASCA热处理后合金的韧性变差。

**关键词：**激光熔覆成形；Ti-5321合金；多重热处理；断裂韧性

作者简介：刘国政，男，1996年生，博士生，西北有色金属研究院，陕西 西安 710016，E-mail：2190035@stu.neu.edu.cn